Noninvasive Assessment of Collagen Gel Microstructure and Mechanics Using Multiphoton Microscopy

Christopher B. Raub,* Vinod Suresh,* Tatiana Krasieva,† Julia Lyubovitsky,† Justin D. Mih,* Andrew J. Putnam,*‡ Bruce J. Tromberg,*†§ and Steven C. George*‡

*Department of Biomedical Engineering, †The Beckman Laser Institute, ‡Department of Chemical Engineering and Materials Science, and §Department of Surgery, University of California Irvine, Irvine, California

ABSTRACT Multiphoton microscopy of collagen hydrogels produces second harmonic generation (SHG) and two-photon fluorescence (TPF) images, which can be used to noninvasively study gel microstructure at depth (~1 mm). The microstructure is also a primary determinate of the mechanical properties of the gel; thus, we hypothesized that bulk optical properties (i.e., SHG and TPF) could be used to predict bulk mechanical properties of collagen hydrogels. We utilized polymerization temperature (4–37°C) and glutaraldehyde to manipulate collagen hydrogel fiber diameter, space-filling properties, and cross-link density. Multiphoton microscopy and scanning electron microscopy reveal that as polymerization temperature decreases (37–4°C) fiber diameter and pore size increase, whereas hydrogel storage modulus (G', from 23 ± 3 Pa to 0.28 ± 0.16 Pa, respectively, mean ± SE) and mean SHG decrease (minimal change in TPF). In contrast, glutaraldehyde significantly increases the mean TPF signal (without impacting the SHG signal) and the storage modulus (16 ± 3.5 Pa before to 138 ± 40 Pa after cross-linking, mean ± SD). We conclude that SHG and TPF can characterize differential microscopic features of the collagen hydrogel that are strongly correlated with bulk mechanical properties. Thus, optical imaging may be a useful noninvasive tool to assess tissue mechanics.

INTRODUCTION

Fibrosis, the abnormal deposition of collagen in response to inflammation, characterizes many diseases including asthma (1–6), atherosclerosis (7–9), dermal keloid (10–12), and cirrhosis (13,14). For example, in asthma subepithelial fibrosis in the airways increases the thickness of the lamina reticularis three- to fivefold, can appear before clinical symptoms, and alters the mechanical properties of the airway, which can, in turn, alter the progression of the disease (4–6). However, characterizing fibrosis in vivo at the cellular and molecular level is currently accomplished by invasive tissue biopsy, and there are no methods to characterize the in vivo microscopic mechanical properties of fibrotic tissue.

Multiphoton microscopy (MPM) is capable of high resolution, three-dimensional imaging of biological tissue to a depth on the order of 1 mm using femtosecond pulses of near-infrared (NIR) laser light. Fibrillar collagen responds to near-infrared laser light with both second harmonic generation (SHG) and two-photon excited fluorescence (TPF) (15,16). SHG relies on a nonabsorptive, nonlinear light-collagen interaction producing light at exactly one-half the excitation wavelength (17,18), and depends upon collagen's structure at the noncentrosymmetric secondary (triple helix) level, and upon molecular packing and scattering on the tertiary (fibril), and quaternary (fibers) levels of organization. In contrast, TPF is an absorptive process, arising from excitation of fluorophores (in collagen, of intramolecular pyridinium-type cross-links and other uncharacterized fluorophores) (19). Thus, simultaneous imaging of SHG and TPF signal reveals additional information about collagen's microstructure and biochemical state than imaging either signal alone, or imaging reflectance signal. Image segmentation, which considers noise and signal-containing pixels separately, can provide quantitative measurements of SHG and TPF image parameters that correlate robustly with microstructural or biochemical features of collagen-containing tissue. Because it is noninvasive and relatively nondamaging, MPM may be a valuable tool for assessing fibrosis and changes in mechanical properties in vivo at the microscopic scale. For example, we have shown that SHG image intensity of lung fibroblast-seeded collagen hydrogels characterizes TGFβ2 dose-dependent changes in the collagen microstructure (20).

In vitro self-assembled collagen hydrogels are extensively used as substrates for tissue engineering (21–26), and have been utilized both in general fibrosis models (27–32) and models of the asthmatic airway (20,31,33–35). Thus, there is potential for SHG and TPF to independently characterize collagen microstructure and mechanical properties of these tissues. Researchers have used MPM to image collagen, elastin, and cells in a variety of ex vivo and in vitro tissues, including tail tendon (36–45), skin (45,46), cornea (47–53), fibroblast-seeded collagen gels (16), tissue-engineered skin equivalents (54), asthma fibrosis models (20), and epithelial cell-seeded tissue equivalents (33). In these studies, SHG provides detailed structural information about collagen, whereas TPF identifies other extracellular matrix components and cells. Both signals may measure relative changes in fibrotic state. Although multiple studies have used MPM to probe the

Submitted September 25, 2006, and accepted for publication December 1, 2006.

Address reprint requests to Steven C. George, MD, PhD, Dept. of Biomedical Engineering, 3120 Natural Sciences II, University of California Irvine, Irvine, CA 92697-2715. Tel.: 949-824-3941; Fax: 949-824-2541; E-mail: scgeorge@uci.edu.

0006-3495/07/03/2212/11 $2.00

doi: 10.1529/biophysj.106.097998

collagen microstructure in vitro and in vivo (37,44,55), there have been no reports describing whether these bulk optical properties provide information on the mechanical properties of the matrix.

Acid-solubilized collagen is known to self-assemble in vitro in a temperature-dependent manner with a sigmoidal reaction curve (56), impacting fibril and fiber dimensions. Lateral and end-to-end monomer polymerization begins from collagen monomers ~1.5 nm wide and 300 nm long that form aggregates of 5–17 molecules (57–59). Hydrophobic interactions stabilize the monomer backbone, whereas covalent bonds (cross-links) form between the nonhelical monomer ends and helical cross-linking sites. Collagen fibrils 15–200 nm wide and fibers (composed of two or more fibrils) may be stabilized with both noncovalent (hydrogen and ion-ion) and covalent bonds (cross-links) (58,60). Both fibril and fiber diameter increase at lower polymerization temperatures (56,61).

The goal of this study was to systematically alter fiber structure and fluorescent cross-link content of collagen hydrogels using polymerization temperature and glutaraldehyde, respectively, and to determine whether changes in collagen gel mechanical properties (i.e., storage and elastic modulus) correlate with changes in the bulk optical properties (i.e., SHG and TPF).

METHODS

Collagen hydrogel preparation

Collagen hydrogels were polymerized by mixing the following components in order on ice: 100 μl 10× phosphate buffered saline ((PBS) Sigma, St. Louis, MO, consisting of 0.1 M phosphate buffer, 1.38 M NaCl, and 0.027 M KCl, pH 7.4), 0.41 ml ddH_2O with 0.025 M sodium hydroxide added (to reach a pH of 12.38), and 0.49 ml 8.16 mg/ml acid-soluble rat tail tendon collagen (BD Biosciences, San Jose, CA). After vortexing, the collagen concentration was 4 mg/ml and pH 7.4. For MPM imaging, the collagen mixture was immediately pipetted into eight-chambered coverglasses (Fisher, Hampton, NH) at 0.1 ml/chamber and incubated for 48 h at four temperatures: 4, 14, 24, and 37°C. Before MPM imaging, half of the four hydrogels prepared at each polymerization temperature were cross-linked with 1 ml 0.2% glutaraldehyde (GTA) for 1 h at 24°C and exhaustively washed with PBS. Cross-linking with this GTA concentration has been found to produce significant changes in collagen hydrogel mechanical properties (62). For rheology, the gels were polymerized directly between the rheometer's (RFSII, Rheometrics, New Castle, DE) testing plates.

Scanning electron microscopy

Because scanning electron microscopy (SEM) has better resolving power than MPM, SHG and TPF microstructure measurements were compared to measurements from SEM images. SEM was performed on collagen hydrogels polymerized at the temperatures listed above using a Phillips XL-30 SEM (Eindhoven, The Netherlands) with a secondary electron detector. The hydrogels were prepared for electron microscopy by fixation followed by serial dehydration with ethanol and hexamethyldisilazane (HMDS). Following polymerization, the hydrogels were fixed with 4% formaldehyde in PBS for 1 h at room temperature. Then, after three 10-min washes in PBS and two 10-min washes in ddH_2O, the hydrogels were transferred to glass vials and further fixed with 1% osmium tetroxide for 1 h at room temperature. After two 10-min washes in ddH_2O, the fixed hydrogels were dehydrated in a graded ddH_2O/ethanol series: 30%, 50%, 70%, 90%, and two 100% ethanol washes for 10 min each. Following the ddH_2O/ethanol washes, the hydrogels were washed with a graded ethanol/HMDS series: 33%, 50%, 66%, and 100% HMDS washes for 15 min each. Finally, the gels were cut in three pieces and allowed to dry overnight on aluminum foil so that the bottom, top, and cross section of the gel were facing up. Then the dried hydrogels were mounted on SEM sample stages using carbon tape and sputter coated with Pd/Au to a thickness of 6 nm using a Polaron SC7620 sputter coater (Watford, UK). The specimens were imaged at 10 kV and magnifications of 2000×, 20,000×, and 100,000×. SEM images were analyzed using NIH ImageJ software (Bethesda, MD). Average fiber diameter was calculated from a random sample of hand-measured fibers in SEM images. Each SEM image had similar contrast and brightness, as well as the same electron beam voltage.

Fiber diameter histograms were constructed by sampling five 2 × 2 μm regions from each of nine 20,000× images of hydrogels formed at the four polymerization temperatures. Fiber diameters were estimated using a line-drawing feature of ImageJ that reports line length in pixels. Fiber diameters were measured roughly at the midpoint of each fiber when that midpoint was discernable; otherwise, the fiber diameter was measured in the middle of the longest discernable part of the fiber. Pixels were converted to standard units of length measurements using SEM image scale bars.

Multiphoton microscopy

SHG and TPF signals from collagen hydrogels were collected in the epi-configuration using a previously described custom-built multiphoton laser scanning microscope (MPM) (16). Two-photon events were created using a mode-locked Ti:Sapphire laser (170-fs pulse width, 76 MHz repetition rate; Mira 900F, Coherent, Palo Alto, CA) pumped by a 5-W Verdi laser (Coherent) producing 770 nm light (16) focused 20 μm into the hydrogel above the coverslip by a 40×, 0.8 numerical aperture water immersion Achroplan objective (Zeiss, Jena, Germany). Average power at the microscope back aperture was 80 mW (corresponding to ~6.7 mW at the sample site). SHG and TPF were collected simultaneously in two separate channels, and the signals were summed over five successive scans. Though SHG primarily copropagates with the laser beam, a significant portion of the forward-propagated SHG undergoes subsequent backscattering and is detectable in the epi-configuration, especially when fibers are larger than the incident wavelength. The SHG signal (emission 385 nm) was collected using a 380/15 nm bandpass filter, whereas TPF (maximum emission 525 nm; (16)) was collected in a second channel using a 520/40 nm bandpass filter. Three to six images per hydrogel were collected from three hydrogels per polymerization temperature, with at least 1 mm separation distance between images in each gel. This experiment was repeated more than three times, both on the custom-built MPM and a commercial model (LSM 510 Meta, Zeiss). For the custom-built microscope, each 16-bit image contained 256 × 256 pixels and a 114 × 114 μm field of view. Pixel sampling rate was 1 kHz (pixel dwell time = 1 ms). Each image was integrated over five frames. SHG and TPF signals were quantified from images using IP Labs software (Scanalytics, Fairfax, VA). The mean and standard deviation of signal intensity per pixel were collected from raw images as well as images processed by segmentation. Segmentation involved finding the maximum value pixel of each signal from a region of interest within each image that contained no discernable collagen, and then setting a threshold just above this pixel intensity (i.e., the noise threshold). Pixels with intensities below the noise threshold were excluded from segmented images. Then, the mean signal intensity per pixel, total signal intensity, and SHG or TPF image fraction of the segmented images were calculated. The image fraction was defined as the number of segmented pixels above the noise threshold divided by the total number of image pixels, and expressed as a percentage. After setting the noise threshold in TPF images, which display a much lower signal/noise ratio than SHG images, segments containing <50 pixels were

discarded. This was found to decrease noise in the segmented TPF images while preserving significant collagen TPF signal. In all other details TPF and SHG images were processed similarly.

Rheology

Collagen gels were tested in a RFSII rheometer (Rheometrics) using dynamic shear mode, parallel plate geometry, and a hydrated chamber as previously described (63). Plate diameter was 25 mm, and the gap between plates was 0.2 mm. Frequency sweeps were conducted, with dynamic strain frequency varying from 0.1 to 100 s^{-1}. Before the frequency sweeps amplitude sweeps were conducted to determine the linear viscoelastic region. Subsequently, all frequency measurements were taken at 5% strain, which falls within the linear viscoelastic region of these hydrogels. Mechanical spectra were obtained for the following variables: storage modulus (G'), loss modulus (G''), and phase angle (δ), where $\tan\delta = G''/G'$, a characterization of the ratio of gel viscous to elastic behavior.

Collagen hydrogel components were mixed together on ice and the resulting solution was immediately pipetted onto the rheometer's lower parallel plate, which was maintained at one of four polymerization temperatures by a water bath. The upper plate was then lowered until the gap between the two plates was 0.2 mm, and the gels were allowed to polymerize between the rheometer plates for a total time of: 20 min (for 37°C gels), 45 min (for 24°C gels), 5 h (for 14°C gels), and 24 h (for 4°C gels). Polymerization was deemed complete both by the turbid appearance of the gel and the cessation of increase of hydrogel storage modulus with time, after which mechanical spectra were immediately collected. Polymerization times were necessarily shorter for rheology than for MPM imaging samples, since evaporation could not be completely prevented while the gels were between the rheometer plates, whereas MPM imaging chambers were sealed. Polymerization lag phase shortens with increasing polymerization temperature, and collagen gels polymerized at the temperatures and times above displayed similar trends in microstructure and MPM image parameter values to corresponding gels polymerized for 48 h before imaging (data not shown). Raising the temperature of the gel before testing had little or no effect on the resulting mechanical spectra.

Statistics

Parameters from SHG, TPF, and SEM images were compared across image conditions using either parametric single-factor ANOVA or nonparametric Kruskal-Wallis ANOVA for the four polymerization temperatures; Student's or Welch's *t*-test to compare chemically uncross-linked and GTA cross-linked collagen gels' optical parameters; and a paired *t*-test to compare shear moduli before and after GTA cross-linking. The statistics g_1 and g_2 were used to estimate symmetry and kurtosis, respectively, of fiber diameter distributions measured from SEM images. These statistics were calculated from the following equations:

$$g_1 = \frac{n\sum(X_i - \overline{X})^3}{(n-1)(n-2)s^3} \quad (1)$$

$$g_2 = \frac{\sum(X_i - \overline{X})^4 n(n+1)/(n-1) - 3[\sum(X_i - \overline{X})^2]^2}{(n-2)(n-3)s^4}, \quad (2)$$

where n is the sample size, X_i are the individual fiber diameter measurements, $\overline{X}$ is the arithmetic mean fiber diameter from SEM images, and s is the sample standard deviation. Statistical significances of symmetry and of kurtosis were determined by previously reported methods that transform g_1 and g_2 into Z-statistics from a standard normal distribution, used to estimate the probability that the samples come from a symmetric and mesokurtic distribution (64). For these tests as well as for ANOVA and *t*-tests, statistical significance resulted if $p < 0.05$. Scores are reported as mean ± SE, except for the GTA cross-linking rheology experiment, where SD replaces SE. SE describes variance in the (normal) distribution of sample means whose average estimates the true mean (for example, Fig. 2), whereas SD describes variance in the (possibly nonnormal) sampling distribution (for example, Fig. 1, *b–e*), or when only a single sample is taken (for example, Fig. 5). All statistical tests were performed using Instat 2.01 (GraphPad Software, San Diego, CA) or in Excel (Microsoft, Redmond, WA) using standard methods (64). Polynomial trendlines were added to figures for visualization purposes only.

RESULTS

Polymerization temperature controls fiber diameter and gel microstructure

SEM reveals larger diameter collagen fibers as polymerization temperature decreases (Fig. 1 *a*, 20,000×); but the SEM images, unlike MPM images (Fig. 3 *a*), reveal parallel-aligned fibrils within fibers (Fig. 1 *a*, 100,000×). Fiber diameter varies across the polymerization temperature conditions because of differences in the number of fibrils per fiber rather than large changes in fibril diameter. Small diameter fibers are visible in SHG (Fig. 3 *a*) and SEM images (Fig. 1 *a*) of gels polymerized at 4 and 14°C, sometimes independent of larger diameter fibers and sometimes emanating from the splayed ends of large diameter fibers. However, SHG and SEM images show that large diameter fibers dominate the space-filling characteristics of the gels polymerized at the two lower temperatures. With increasing polymerization temperature the hydrogels display a finer and more homogeneous network of fibers.

As polymerization temperature increases from 4 to 37°C maximum fiber diameter decreases ~70% from >1.1 μm to <320 nm, while the arithmetic mean fiber diameter decreases proportionally, ~70% from 218 to 62 nm (Fig. 1, *a–d*). Gels polymerized at colder temperatures also had greater ranges in fiber diameters. The range of the fiber diameters was 1083 nm for 4°C-polymerized gels ($n = 233$ fibers) and 132 nm for 37°C-polymerized gels ($n = 605$ fibers). The fiber diameter distributions are right-tailed and leptokurtic (i.e., weighted about the mean and tails compared to a normal distribution), with both $g_1 > 0$ ($p < 0.0001$; indicated by *, Fig. 1, *b–e*) and $g_2 > 0$ ($p < 0.002$; indicated by #, Fig. 1, *b–e*). Histograms of SHG fiber diameters were also constructed (data not shown), with means and standard deviations listed in Fig. 2. These histograms look Gaussian, but are centered around larger apparent mean fiber diameters than the SEM histograms by ~1 order of magnitude. The variation between polymerization temperatures of SHG fiber diameter means was found to be significantly greater than expected by chance (parametric single-factor ANOVA on reciprocal-transformed data to produce homoscedasticity, $p < 0.0001$, $n = 107$; indicated by *, Fig. 2). The variation between polymerization temperatures of SEM fiber diameter medians was also found to be significantly greater than expected by chance (nonparametric Kruskal-Wallis ANOVA, $p < 0.0001$, $n = 233$; indicated by #, Fig. 2). The SHG mean fiber diameters, d_{SHG}, were plotted against SEM mean fiber

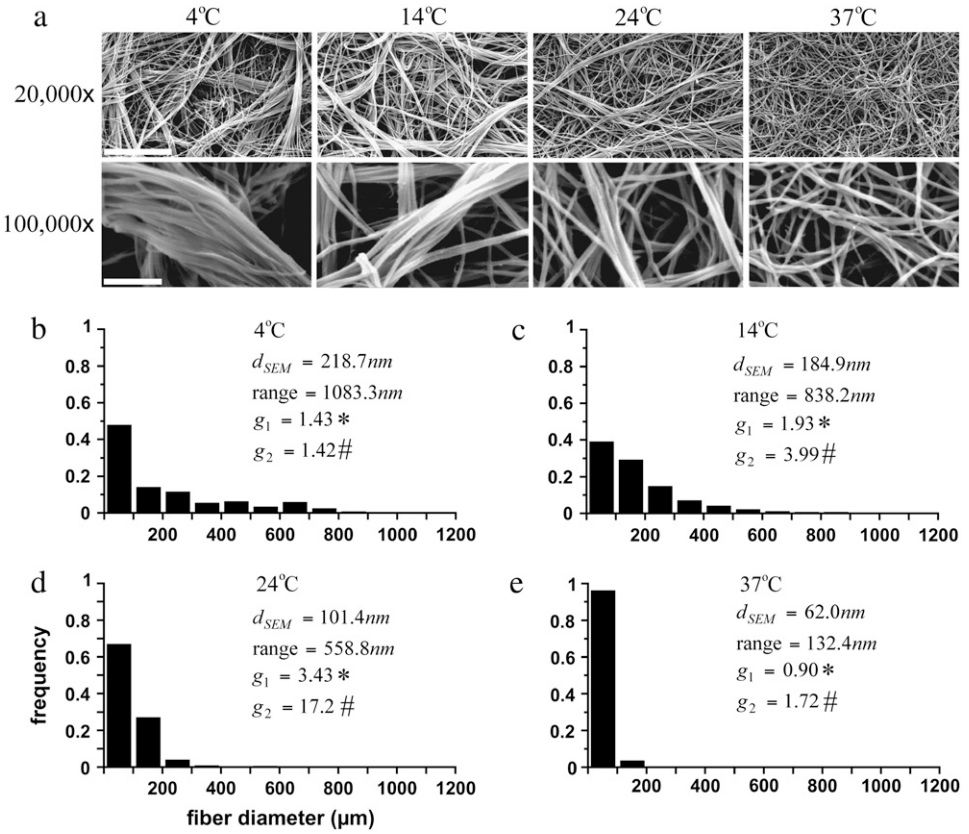

FIGURE 1 (*a*) SEM reveals collagen fiber dimensions (20,000× SEM images, bar represents 3 μm) and fibrils within each fiber (100,000× images, bar represents 500 nm). (*b–e*) Fiber diameter histograms constructed from SEM image measurements show polymerization temperature-shifted distributions. The corresponding mean, range, symmetry statistic g_1, and kurtosis statistic g_2 are listed above each histogram. Nine SEM images were sampled per polymerization temperature, with n = 233, 598, 605, and 600 fibers for 4, 14, 24, and 37°C polymerization conditions, respectively.

diameters, d_{SEM}, for each polymerization condition; a linear regression of d_{SHG} on d_{SEM} shows a strong linear correlation (R^2 = 0.938) with a slope of ~10.8 and a y-intercept of ~0.62 μm (Fig. 2), which is close to the lateral image resolution (~0.45 μm).

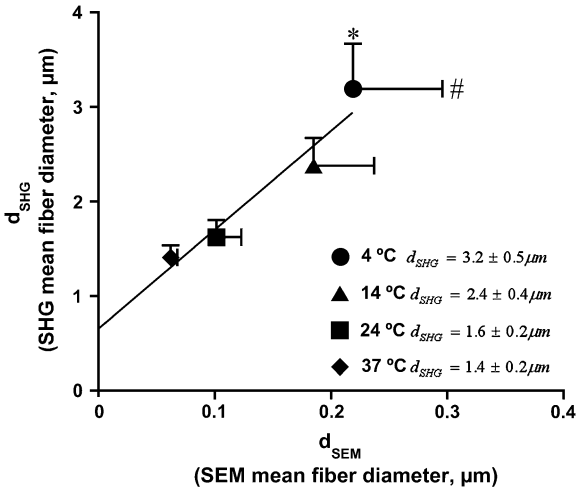

FIGURE 2 The arithmetic mean fiber diameters from SEM images, d_{SEM}, correlate with mean fiber diameters measured from SHG images, d_{SHG}, for each polymerization temperature imaged (error bars represent mean ± SE). Mean SHG fiber diameters ± SE are listed in the figure, with 10, 6, 6, and 6 images sampled and n = 107, 187, 195, and 208 fiber diameters counted for the 4, 14, 24, and 37°C polymerization conditions, respectively.

SHG and TPF from collagen gels vary with microstructure

Collagen SHG and TPF were imaged both with a LSM 510 Meta (Zeiss) and a custom-built MPM, yielding similar results. For clarity, only results from the custom-built MPM are presented. Fig. 3 demonstrates that SHG and TPF signals from collagen hydrogels are strongly dependent on polymerization temperature, and are both independent and overlapping (colocalizing). The SHG and TPF signals were false-colored blue (for SHG) and green (for TPF) and were overlaid to compare the signals' spatial distribution (Fig. 3 *a*). Signal/noise ratios and total signal were higher for SHG than for TPF within each image. MPM images of 4°C-polymerized gels show most clearly that: 1), SHG and TPF overlap in regions where fibers are lying in the lateral plane of the image; and 2), more TPF than SHG is collected from punctate regions roughly the diameter of collagen fibers in cross section.

Colder polymerization temperatures produced loosely packed, thicker collagen fibers with brighter SHG (assessed by mean SHG from segmented images, Fig. 3 *b*), larger pores between fibers (Fig. 3 *a*), and a smaller SHG image fraction (Fig. 3 *c*). Conversely, warmer polymerization temperatures produced thinner and dimmer, but more abundant and closely spaced collagen fibers.

Mean SHG intensity from segmented images (Fig. 3 *b*) correlates well with polymerization temperature and drops

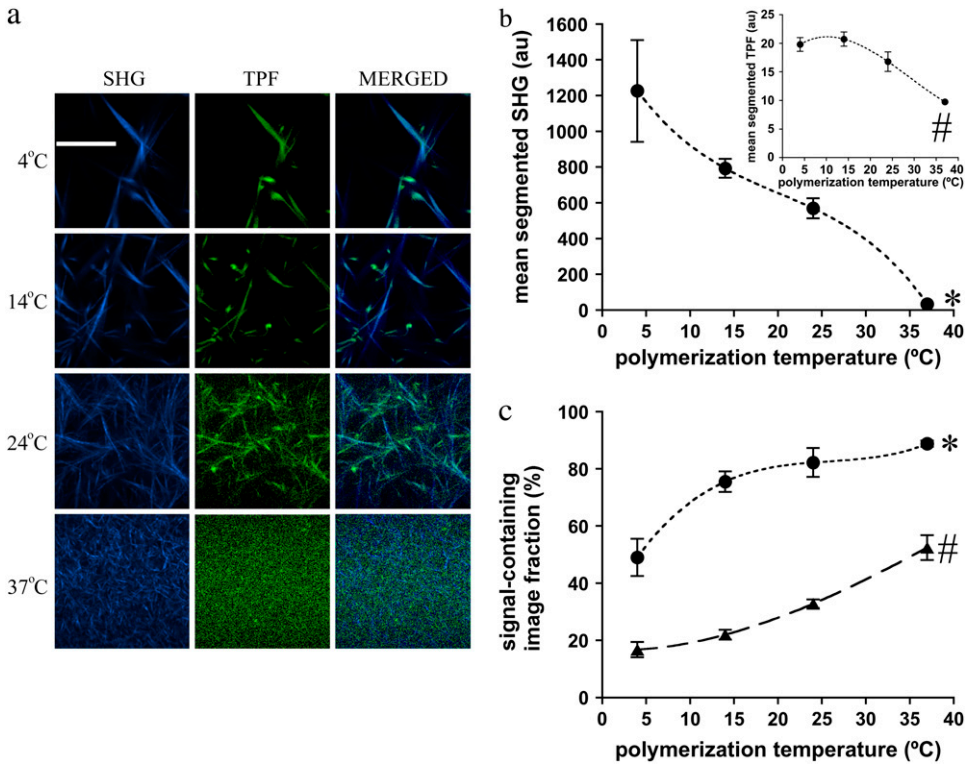

FIGURE 3 (*a*) Simultaneously collected SHG (*leftmost column*, *blue* palette) and TPF (*middle column*, *green* palette) images of collagen hydrogels polymerized at various temperatures. Merged images (*rightmost column*) compare and contrast SHG and TPF signal intensities and spatial organization. Images are 256 × 256 pixels, and 114 μm on a side. n = 10, 6, 6, and 6 images for the 4, 14, 24, and 37°C conditions, respectively, were used for quantification and statistical analysis. Bar represents 50 μm. Mean SHG (*b*) and TPF (*b*, *inset*) calculated from segmented images vary with polymerization temperature. (*c*) SHG (●) and TPF (▲) image fraction calculated from noise-thresholded images also vary with polymerization temperature. Polynomial trendlines have been added as a visual aid.

~97% from 4 to 37°C (1227 ± 285 to 33.8 ± 2.7 arbitrary units, au). In contrast, the mean TPF intensity from segmented images is much less sensitive to microstructure: the mean segmented TPF for 37°C polymerized gels (9.75 ± 0.03 au) is only slightly dimmer (~50%) compared to the 4°C (19.8 ± 1.2 au) condition (Fig. 3 *b*, *inset*). The variation between conditions of mean SHG and TPF from segmented images was found to be significantly greater than expected by chance (nonparametric Kruskal-Wallis ANOVA test, $p < 0.0001$ and $p = 0.0123$ for SHG and TPF data, respectively; indicated by * and #, Fig. 3 *b*).

For 4°C-polymerized gels, the ratio of mean segmented SHG/TPF is 59 ± 11 but this ratio decreases sharply to 3.3 ± 0.2 for 37°C-polymerized gels (calculated from data in Fig. 3 *b* and *inset*). The mean of the maximum SHG pixel intensities from each image has a trend similar to the mean segmented SHG, while the maximum TPF pixel intensity shows no such correlation (data not shown).

The SHG image fraction increased from 49.0 ± 6.5% to 88.8 ± 1.1% between 4°C- and 37°C-polymerized gels (Fig. 3 *c*, *solid circles*). Similarly, the TPF image fraction correlates positively with polymerization temperature, and increased from 16.8 ± 2.7% to 52.5 ± 4.3% between 4°C and 37°C-polymerized gels (Fig. 3 *c*, *solid triangles*). Unlike the SHG image fraction, the TPF image fraction does not begin to plateau at the 37°C polymerization condition. The variation between polymerization conditions of SHG image fraction and likewise the variation between conditions of TPF image fraction were found to be significantly greater than expected by chance (parametric single-factor ANOVA, $p < 0.0001$ for both mean SHG and TPF image fraction; indicated by * and #, Fig. 3 *c*).

G′ and *G″* vary with microstructure

Typical values of the storage (G') and elastic (G'') modulus for the four polymerization conditions, measured for dynamic strain frequencies from 0.1 to 100 rad/s, are shown in Fig. 4 *a*. The shear moduli display frequency independence over this range, confirming previous studies (63,65). Mean G' increases with polymerization temperature, roughly two orders of magnitude, from 0.3 ± 0.2 Pa for 4°C-polymerized gels to 22.7 ± 2.3 Pa for 37°C-polymerized gels (Fig. 4 *b*). G'' increases in parallel with G' as has been previously reported for collagen hydrogels (65). The variation between polymerization temperatures of median G' was found to be significantly greater than expected by chance (nonparametric Kruskal-Wallis ANOVA, $p < 0.0001$, $n = 89$; indicated by *, Fig. 4 *b*). Median G'' from each polymerization temperature were similarly statistically significant (nonparametric Kruskal-Wallis ANOVA, $p < 0.0001$, $n = 89$; indicated by #, Fig. 4 *b*).

GTA cross-linking affects TPF, *G′*, and *G″*

Fig. 5 demonstrates the impact of GTA-induced cross-linking on the SHG and TPF signals. Comparing MPM images of chemically uncross-linked to GTA cross-linked collagen gels shows that GTA cross-linking significantly increases the total and mean segmented TPF signal (49,000 ± 4000 au to

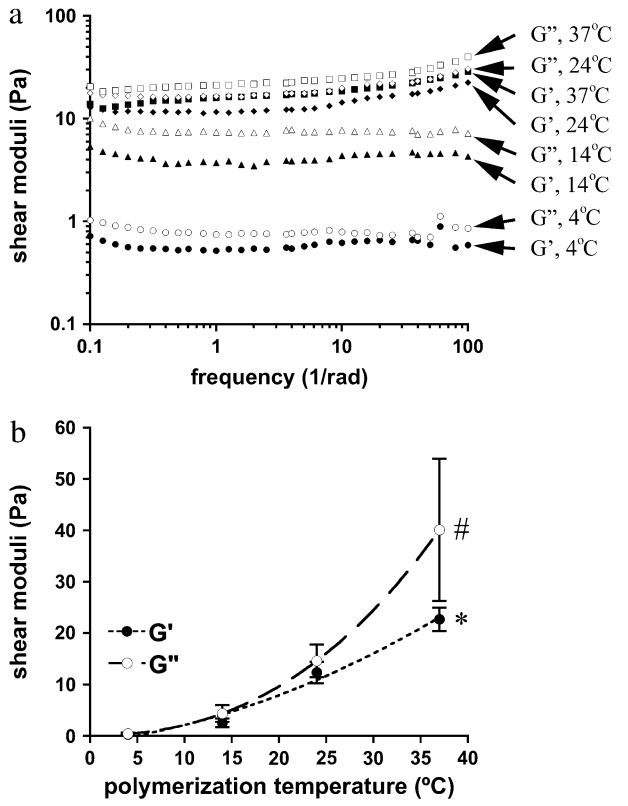

FIGURE 4 G' and G'' vary with polymerization temperature over a range of strain frequencies. (*a*) Representative frequency sweeps of G' (*solid symbols*) and G'' (*open symbols*) at each polymerization temperature. (*b*) Mean G' (*solid symbols*) and G'' (*open symbols*) from multiple frequency sweeps ($n = 3$ gels/polymerization temperature, 31 frequencies per sweep) steadily increase between 4 and 37°C. Polynomial trendlines have been added as a visual aid.

150,000 ± 6000 au and 8.9 ± 0.2 to 12.4 ± 0.1 au, respectively, Fig. 5, *c* and *d*) but does not change SHG intensity from the collagen fibers: 156.1 ± 8.9 au to 163.0 ± 8.2 au (mean SHG from unprocessed images). The TPF image fraction also increased significantly from 8.3 ± 0.6% to 18.5 ± 0.8% (Fig. 5 *d*). Statistical tests confirm TPF parameter increases upon GTA cross-linking (Student's *t*-test, $p < 0.0001$, $n = 10$ images from three gels; Welch's modified *t*-test, $p < 0.0001$, $n = 10$ images from three gels; and Student's unpaired *t*-test, $p < 0.0001$, $n = 10$ images from three gels, for total segmented TPF, mean segmented TPF, and TPF image fraction comparisons, respectively; indicated by * and #, Fig. 5, *c* and *d*).

TPF signal augmentation by GTA cross-linking occurs simultaneously with almost 10-fold increases in G' (16.0 ± 3.5 Pa to 137.6 ± 39.0 Pa) and G'' (13.1 ± 8.1 Pa to 101.7 ± 59.9 Pa) (Fig. 5 *e*). Meanwhile, tan δ ($=G''/G'$) decreases after 1 h of cross-linking from 1.15 ± 0.64 to 0.63 ± 0.24 ($n = 3$). The difference in mean G' between chemically uncross-linked and GTA cross-linked collagen gels was found to be statistically significant (paired *t*-test, $p = 0.0034$, $n = 4$; indicated by *, Fig. 5 *e*). The difference in median G'' between chemically uncross-linked and GTA cross-linked collagen gels (which displays more variation than G' data) was found to be statistically significant (Mann-Whitney test, $p = 0.0143$, $n = 4$; indicated by #, Fig. 5 *e*).

Gel mechanical properties correlate with optical parameters

Varying the polymerization temperature of 4 mg/ml collagen hydrogels systematically changed the fiber volume fraction and space-filling characteristics as well as the bulk shear moduli. The shear moduli G' and G'' correlate positively with TPF and SHG image fraction for these gels (Fig. 6, *a* and *b*), although the correlation between the shear moduli and SHG image fraction is most linear for the 14–37°C polymerization conditions. In contrast, the shear moduli correlate negatively with mean segmented TPF and SHG signal for 4 mg/ml collagen gels with polymerization temperature-controlled microstructure (Fig. 6, *c* and *d*). Since all gels contained 4 mg/ml collagen content, gels with larger diameter fibers contained fewer fibers and larger pores, linking the mechanical and optical properties of the gels.

DISCUSSION

A noninvasive, nonperturbing method to assess the mechanical properties of the matrix does not exist, yet alterations in these mechanical properties profoundly impact both macroscopic (6,66) and microscopic (67–70) biology. Our study is the first to our knowledge to assess the potential of using multiphoton microscopy to characterize the mechanical properties of collagen hydrogels (models of the extracellular matrix). Both SHG and TPF are sensitive to alterations in the microscopic structure of the gel and intermolecular cross-links induced by polymerization temperature and glutaraldehyde, respectively. Furthermore, the SHG and TPF signals correlate strongly with microstructure and with GTA cross-link induced changes in the mechanical properties suggesting that MPM may be a useful tool to noninvasively probe matrix mechanics.

We have measured distinct microstructural changes induced by polymerizing acid-solubilized rat tail tendon collagen at different temperatures (thus impacting the polymerization time) while keeping the mass content of collagen constant. In particular, fiber diameters assessed by MPM and SEM increased with decreasing temperature. This observation is likely due to the self-assembly properties of collagen and to polymerization kinetics, in which polymerization temperature affects the balance of hydrophobic, electrostatic, and hydrogen bond forces between polymerizing collagen monomers and fibrils, thus favoring lateral fibril and fiber growth more at lower temperatures than at higher temperatures. Specifically, lowering the polymerization temperature weakens hydrophobic attractive forces (71).

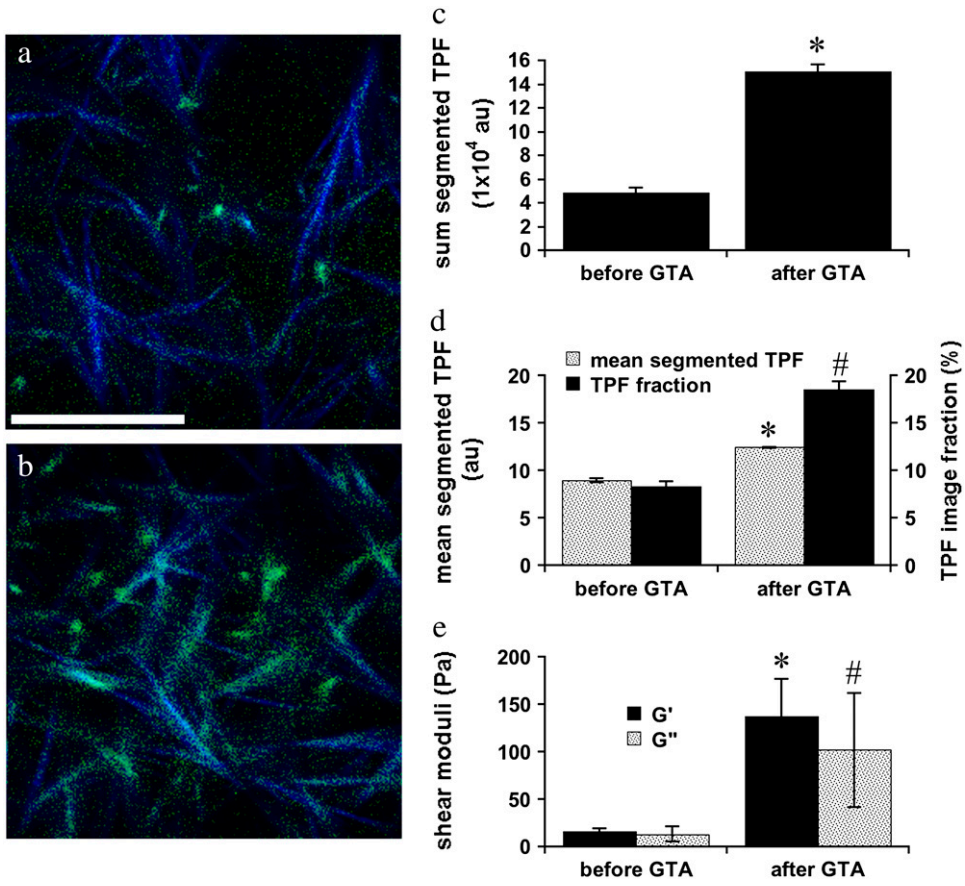

FIGURE 5 Collagen hydrogels (4 mg/ml) polymerized at 24°C exhibit altered TPF signal (*green* palette) with (*b*) compared to without (*a*) GTA cross-linking in 0.2% GTA/PBS for 1 h, but SHG signal (*blue* palette) remains unchanged (bar represents 50 μm). GTA cross-linking affects the mean sum of TPF pixel intensities per segmented image (*c*), mean TPF pixel intensity from segmented images (*d*, *shaded bars*), mean TPF image fraction (*d*, *solid bars*), mean G' (*e*, *solid bars*), and mean G'' (*e*, *shaded bars*). Error bars represent SD.

This study utilizes a cold-start polymerization, bringing acid-soluble rat tail tendon collagen to near-neutral pH (7.4), allowing polymerization to slowly occur at 4°C or increasing temperature to speed polymerization. Our study confirms previous results by Christiansen et al. (72), who polymerized collagen similarly and measured fibril diameters with TEM ranging from ~10–120 nm, with mean diameters ~22 nm for collagen polymerized at pH 7.5 and temperature 25–37°C (values roughly similar to this study, data not shown). Fibril diameters increased at lower polymerization pH but showed no dependence on polymerization temperature, similar to our results. Unlike this study, fibers composed of aggregated fibrils were not measured. In contrast, a study by Wood and Keech on bovine dermal collagen self-assembled under warm-start conditions (acid-solubilized collagen equilibrated at 25°C before neutralization with NaOH-KH_2PO_4 buffer to form a gel at I 0.23 and pH 7.1) showed fibril and fiber diameter increases with decreasing polymerization temperature, from 37°C to 21°C (56). In this study, under 37°C-polymerization conditions, fibril diameters ranged from 20 to 120 nm with mode 50 nm, closely overlapping our findings and that of Christiansen et al. (72). But with decreasing polymerization temperature fibril diameters increased, with a range of 180–480 nm and mode 250 nm at 21°C. Also, micron-scale fibril aggregates formed at 25°C and 21°C but not at 37°C, mirroring the thermally irreversible fibril aggregation into fibers observed in this study. We conclude that in our system, polymerization temperature affects fiber but not fibril diameter, but that both fibril and fiber diameter may depend upon collagen source and polymerization method.

Collagen structures slightly smaller than the SHG wavelength (385 nm) should emit and scatter SHG predominantly forward, both because of their size and packing within the focal volume, which leads to destructive interference of back-propagated SHG (36). Fibers much larger than 385 nm, like those polymerized at 4 and 14°C, should backscatter more SHG. Our results—that mean SHG and TPF per collagen-containing pixel increase with increasing fiber diameter—confirm these arguments, as well as previous studies that measure forward and backward-propagated SHG signals from tail tendon collagen (36,43).

Collagen SHG, unlike TPF, has been shown to depend on the fiber orientation with respect to the laser polarization and propagation directions (36,41). Specifically, fibers roughly the same diameter as the SHG wavelength emit SHG exclusively in the forward direction (15,36,43,73). SHG is generated from a hollow shell near fibril surfaces (43) and at fiber interfaces (16), where reflection and scattering can change SHG propagation direction and create back-propagated SHG. In contrast, TPF from fluorescent cross-links in

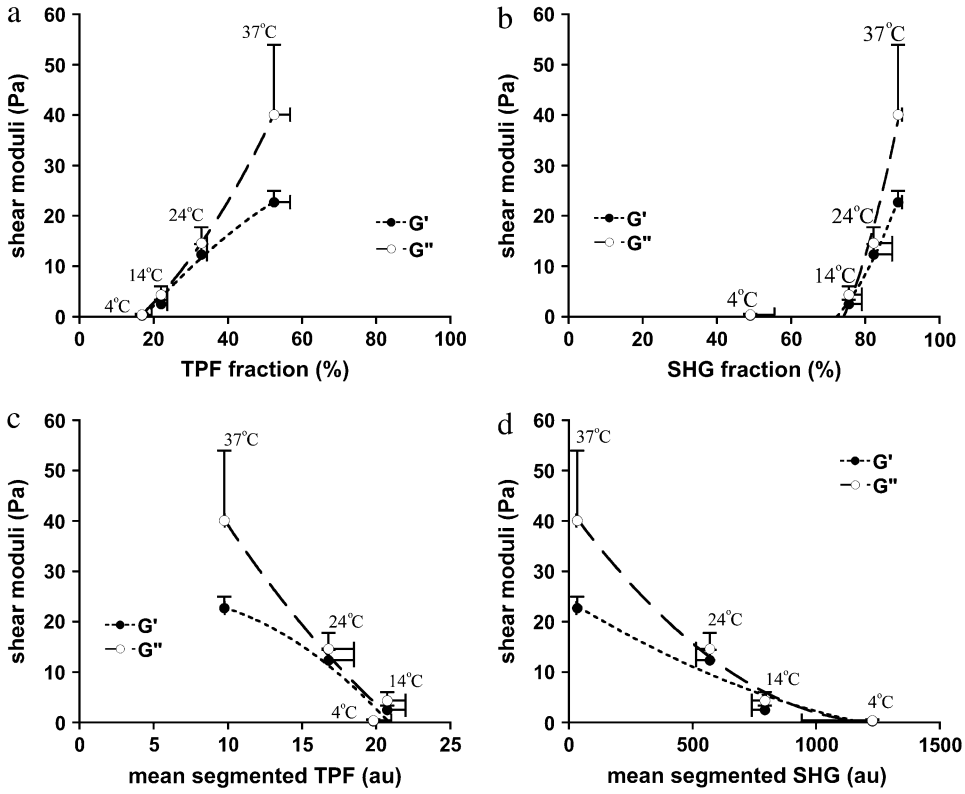

FIGURE 6 Mean G' (*solid symbols*) and G'' (*open symbols*) of collagen gels with temperature-controlled microstructure display positive correlations with TPF (*a*) and SHG image fraction (*b*), but negative correlations with mean TPF (*c*) and mean SHG from segmented images (*d*). All gels contained 4 mg/ml collagen content. Polymerization temperatures are indicated above data points. Error bars represent SE. Polynomial trendlines have been added as a visual aid.

collagen will radiate isotropically and regardless of fiber orientation. Thus, collagen fibers transverse to the image plane of MPM should exhibit stronger TPF and relatively weaker SHG (because the fiber interface is parallel to the SHG propagation direction), whereas fibers within the image plane will exhibit stronger SHG due to backscattering at the fiber interfaces (Fig. 3 *a*).

The polymerization temperature-controlled microstructural trends observed by SHG were validated by SEM. The primary difference is the higher resolution attained by SEM imaging (the Rayleigh resolution limit for our SHG images is ~415 nm (36)). Our results suggest that fiber diameters observed by SHG are approximately an order of magnitude larger than SEM (Fig. 2, *b–f*). Collagen fibrils closely bind water in hydrogels (25,71). Dehydration and fixation of collagen gels can decrease pore size and fiber diameters (38). In addition, SHG and TPF signals carry additional information than just fiber-level physical dimensions. Fibril, monomer, and α-chain configurations affect SHG (44,45), whereas fluorescent cross-links (19,74) can create TPF. As such, the two signals can provide structural information similar to SEM, yet also provide unique and independent data about multiple microscopic levels of collagen organization and composition.

SHG signal drops more steeply than TPF signal as fibers become smaller with increasing polymerization temperature. Several physical phenomena may explain this difference. As previously mentioned, most back-propagated SHG results from secondary scattering of forward-directed SHG photons. Small diameter fibers backscatter less than large diameter fibers (61), suggesting that gels polymerized at higher temperature backscatter less SHG. In contrast, TPF emits isotropically due to the process of photon absorption. Thus, a greater fraction of unscattered TPF than SHG photons are collected in the epi-configuration, which may explain TPF's relative insensitivity compared with SHG to microstructural changes of the collagen network that affect tissue scattering properties. Secondly, SHG's dependence on the square of dipole concentration versus TPF's linear dependence on fluorophore concentration may also explain the differences in sensitivity of the two signals to collagen hydrogel microstructure (75,76). More collagen monomers may be simultaneously exposed to the laser focal volume in a large fiber than a smaller fiber (36), which would tend to increase SHG signal more than TPF signal from the corresponding fluorophores within the same focal volume. Thirdly, parallel-aligned adjacent fibrils may enhance SHG signal from larger diameter fibers polymerized at colder temperatures compared to smaller diameter fibers with less alignment (40). Glycerol-induced fiber dissociation in rat tail tendon reduces back-propagated SHG (44) and forward-propagated SHG (39); lyotropic swelling of rat tail tendon similarly reduces SHG intensity (42), suggesting that collagen alignment and spacing within fibers affects SHG signal intensity.

Two rheological parameters were measured: storage modulus, G', and loss modulus, G''. These two parameters reflect

the amount of energy stored elastically in the collagen network and the amount of energy dissipated through viscous effects, respectively. Altering the collagen hydrogel microstructure allows one to specifically study how this microstructure affects tissue optical and mechanical properties. Recently, a study has correlated increased collagen concentration and polymerization pH with increasing hydrogel linear tensile modulus (77). These researchers used confocal reflection microscopy to measure fiber diameter and qualitatively assess fiber length and number density as a function of polymerization conditions.

This study positively correlates SHG and TPF image fraction with the storage and elastic moduli (Fig. 6, *a* and *b*), but negatively correlates mean segmented SHG and TPF intensity with the storage and elastic moduli (Fig. 6, *c* and *d*). Although fiber diameter may impact fiber stiffness directly, it is perhaps more important to note that relatively few large fibers polymerize at colder temperatures compared to the large number of thinner fibers that polymerize at warmer temperatures. As such, the volume fraction of fibers rather than fiber thickness dominates the bulk mechanical properties. This observation is consistent with other in vitro observations in which a more interconnected and continuous network displays enhanced mechanical properties (77), as well as with in vivo studies that report increased volume fraction of collagen fibers in stiff fibrotic tissue surrounding coronary emboli in rats (66).

In contrast, the mean fiber diameter—but not the volume fraction of fibers—determines the mean segmented SHG. The collagen matrix's space-filling characteristics are important in determining the total SHG and TPF signals, but segmenting the images and averaging the segmented pixels' intensities isolates the effect of fiber diameter from fiber volume fraction. These correlations define a relationship between SHG and TPF image parameters and shear moduli of acellular collagen hydrogels and identify specific components of collagen hydrogel microstructure that can be monitored with SHG or TPF image parameters.

Total and mean segmented TPF correlate strongly with the presence of fluorescent cross-links created by GTA cross-linking. GTA cross-links proteins through many pathways, including the reaction of aldehyde functional groups with ϵ-amino groups primarily from lysine (78,79). Some cross-linking pathways have been proposed that produce a fluorescent pyridinium-type cross-link, whose existence has been confirmed experimentally (74,78,80). Cross-linking simultaneously increased mean TPF and G' and decreased the phase angle of hydrogels exposed to GTA for 1 h. This observation confirms earlier observations in which cross-linked networks display enhanced mechanical properties (78).

Most in vivo fibrosis, like asthmatic subepithelial fibrosis, consists of various fibrillar collagens (often types I, III, and V) (1) that emit SHG, and other components that autofluoresce (i.e., elastin and cells) and scatter light. The noninvasive quality and unique probing of collagen makes simultaneous SHG/TPF imaging superior to conventional tissue biopsy. However, the contributions of tissue scattering and noncollagen signals to MPM image parameters must be understood, as well as the relationship between bulk tissue mechanical properties and the microstructure of collagen and other extracellular matrix components. Despite these challenges, three-dimensional MPM imaging of shallow fibrosis, combined with image processing to analyze colocalized SHG and TPF from collagen may reveal information about collagen fiber alignment, diameter, number density, and cross-link content, which potentially play an important role in determining mechanical properties of fibrosis.

In conclusion, we have demonstrated the ability to systematically and independently alter collagen hydrogel microstructure and cross-link content (and thus optical and mechanical properties) by polymerization temperature and glutaraldehyde cross-linking, respectively. Backscattered SHG intensity, segmented to control for varying fiber numbers and densities within images, correlates positively with mean fiber diameter, whereas bulk hydrogel shear moduli G' and G'' correlate negatively with mean segmented SHG intensity, but positively with SHG image fraction. Back-propagated TPF intensity is less sensitive to these microstructural changes, but increases as hydrogel shear moduli increase and phase angle decreases with GTA cross-linking. These correlations are consistent with models of SHG and TPF production and scattering within collagen hydrogels, and have direct applicability toward noninvasively assessing the mechanical properties of collagen-based tissues.

We thank Dr. Zifu Wang, Leacky Liaw, Wen-An Chen, Larry Lai, Theresa McIntire, and Dr. Hank Oviatt for technical expertise and for assistance in the MPM, SEM, and rheological measurements.

This work was supported, in part, by the National Heart Lung and Blood Institute (HL067954, SCG) and the Air Force Office of Scientific Research (FA9550-04-1-0101). This work was made possible, in part, through access to the Laser Microbeam and Medical Program (LAMMP) at the University of California, Irvine. The LAMMP facility is supported by the National Institutes of Health under a grant from the National Center for Research Resources (NIH No. P41RR01192, BJT).

REFERENCES

1. Roche, W. R., R. Beasley, J. H. Williams, and S. T. Holgate. 1989. Subepithelial fibrosis in the bronchi of asthmatics. *Lancet.* 1:520–524.
2. Jeffery, P. K., R. W. Godfrey, E. Adelroth, F. Nelson, A. Rogers, and S. A. Johansson. 1992. Effects of treatment on airway inflammation and thickening of basement membrane reticular collagen in asthma. A quantitative light and electron microscopic study. *Am. Rev. Respir. Dis.* 145:890–899.
3. Wilson, J. W., and X. Li. 1997. The measurement of reticular basement membrane and submucosal collagen in the asthmatic airway. *Clin. Exp. Allergy.* 27:363–371.
4. Bai, T. R., and D. A. Knight. 2005. Structural changes in the airways in asthma: observations and consequences. *Clin. Sci. (Lond.).* 108:463–477.
5. Karjalainen, E. M., A. Lindqvist, L. A. Laitinen, T. Kava, A. Altraja, M. Halme, and A. Laitinen. 2003. Airway inflammation and basement membrane tenascin in newly diagnosed atopic and nonatopic asthma. *Respir. Med.* 97:1045–1051.

6. Tschumperlin, D. J., and J. M. Drazen. 2006. Chronic effects of mechanical force on airways. *Annu. Rev. Physiol.* 68:563–583.
7. Katsuda, S., and T. Kaji. 2003. Atherosclerosis and extracellular matrix. *J. Atheroscler. Thromb.* 10:267–274.
8. Katsuda, S., Y. Okada, T. Minamoto, Y. Oda, Y. Matsui, and I. Nakanishi. 1992. Collagens in human atherosclerosis. Immunohistochemical analysis using collagen type-specific antibodies. *Arterioscler. Thromb.* 12:494–502.
9. Stary, H. C., A. B. Chandler, R. E. Dinsmore, V. Fuster, S. Glagov, W. Insull Jr., M. E. Rosenfeld, C. J. Schwartz, W. D. Wagner, and R. W. Wissler. 1995. A definition of advanced types of atherosclerotic lesions and a histological classification of atherosclerosis. A report from the Committee on Vascular Lesions of the Council on Arteriosclerosis, American Heart Association. *Arterioscler. Thromb. Vasc. Biol.* 15:1512–1531.
10. Al-Attar, A., S. Mess, J. M. Thomassen, C. L. Kauffman, and S. P. Davison. 2006. Keloid pathogenesis and treatment. *Plast. Reconstr. Surg.* 117:286–300.
11. Doyle-Lloyd, D. J., and J. A. White. 1991. Keloids. *J. La. State Med. Soc.* 143:9–12.
12. Ehrlich, H. P., A. Desmouliere, R. F. Diegelmann, I. K. Cohen, C. C. Compton, W. L. Garner, Y. Kapanci, and G. Gabbiani. 1994. Morphological and immunochemical differences between keloid and hypertrophic scar. *Am. J. Pathol.* 145:105–113.
13. Friedman, S. L., D. C. Rockey, R. F. McGuire, J. J. Maher, J. K. Boyles, and G. Yamasaki. 1992. Isolated hepatic lipocytes and Kupffer cells from normal human liver: morphological and functional characteristics in primary culture. *Hepatology.* 15:234–243.
14. Tsukada, S., C. J. Parsons, and R. A. Rippe. 2006. Mechanisms of liver fibrosis. *Clin. Chim. Acta.* 364:33–60.
15. Zipfel, W. R., R. M. Williams, R. Christie, A. Y. Nikitin, B. T. Hyman, and W. W. Webb. 2003. Live tissue intrinsic emission microscopy using multiphoton-excited native fluorescence and second harmonic generation. *Proc. Natl. Acad. Sci. USA.* 100:7075–7080.
16. Zoumi, A., A. Yeh, and B. J. Tromberg. 2002. Imaging cells and extracellular matrix in vivo by using second-harmonic generation and two-photon excited fluorescence. *Proc. Natl. Acad. Sci. USA.* 99: 11014–11019.
17. Hellwarth, R., and P. Christensen. 1974. Nonlinear optical microscopic examination of structure in polycrystalline ZnSe. *Opt. Commun.* 12: 318–322.
18. Sheppard, C. J. R., J. N. Gannaway, R. Kompfner, and D. Walsh. 1977. The scanning harmonic optical microscope. *IEEE J. Quantum Electron.* 13:D100.
19. Theodossiou, T., G. S. Rapti, V. Hovhannisyan, E. Georgiou, K. Politopoulos, and D. Yova. 2002. Thermally induced irreversible conformational changes in collagen probed by optical second harmonic generation and laser-induced fluorescence. *Lasers Med. Sci.* 17: 34–41.
20. Thompson, H. G., J. D. Mih, T. B. Krasieva, B. J. Tromberg, and S. C. George. 2006. Epithelial-derived TGF-{beta}2 modulates basal and wound healing subepithelial matrix homeostasis. *Am. J. Physiol. Lung. Cell Mol. Physiol.* 291:L1277–L1285.
21. Auger, F. A., M. Rouabhia, F. Goulet, F. Berthod, V. Moulin, and L. Germain. 1998. Tissue-engineered human skin substitutes developed from collagen-populated hydrated gels: clinical and fundamental applications. *Med. Biol. Eng. Comput.* 36:801–812.
22. Lee, C. H., A. Singla, and Y. Lee. 2001. Biomedical applications of collagen. *Int. J. Pharm.* 221:1–22.
23. Wallace, D. G., J. M. McPherson, L. Ellingsworth, L. Cooperman, R. Armstrong, and K. A. Piez. 1988. Injectable collagen for tissue augmentation. *In* Collagen. M. E. Nimni, editor. CRC Press, Boca Raton, FL. 117–144.
24. Wallace, D. G., and J. Rosenblatt. 2003. Collagen gel systems for sustained delivery and tissue engineering. *Adv. Drug Deliv. Rev.* 55:1631–1649.
25. Rosenblatt, J., B. Devereux, and D. G. Wallace. 1992. Effect of electrostatic forces on the dynamic rheological properties of injectable collagen biomaterials. *Biomaterials.* 13:878–886.
26. Silver, F. H., and G. Pins. 1992. Cell growth on collagen: a review of tissue engineering using scaffolds containing extracellular matrix. *J. Long Term Eff. Med. Implants.* 2:67–80.
27. Bell, E., B. Ivarsson, and C. Merrill. 1979. Production of a tissue-like structure by contraction of collagen lattices by human fibroblasts of different proliferative potential in vitro. *Proc. Natl. Acad. Sci. USA.* 76:1274–1278.
28. Redden, R. A., and E. J. Doolin. 2003. Collagen crosslinking and cell density have distinct effects on fibroblast-mediated contraction of collagen gels. *Skin Res. Technol.* 9:290–293.
29. Tomasek, J. J., and S. K. Akiyama. 1992. Fibroblast-mediated collagen gel contraction does not require fibronectin-alpha 5 beta 1 integrin interaction. *Anat. Rec.* 234:153–160.
30. Zhu, Y. K., T. Umino, X. D. Liu, H. J. Wang, D. J. Romberger, J. R. Spurzem, and S. I. Rennard. 2001. Contraction of fibroblast-containing collagen gels: initial collagen concentration regulates the degree of contraction and cell survival. *In Vitro Cell. Dev. Biol. Anim.* 37:10–16.
31. Choe, M. M., P. H. Sporn, and M. A. Swartz. 2003. An in vitro airway wall model of remodeling. *Am. J. Physiol. Lung Cell. Mol. Physiol.* 285:L427–L433.
32. Turley, E. A., C. A. Erickson, and R. P. Tucker. 1985. The retention and ultrastructural appearances of various extracellular matrix molecules incorporated into three-dimensional hydrated collagen lattices. *Dev. Biol.* 109:347–369.
33. Agarwal, A., M. L. Coleno, V. P. Wallace, W. Y. Wu, C. H. Sun, B. J. Tromberg, and S. C. George. 2001. Two-photon laser scanning microscopy of epithelial cell-modulated collagen density in engineered human lung tissue. *Tissue Eng.* 7:191–202.
34. Chakir, J., N. Page, Q. Hamid, M. Laviolette, L. P. Boulet, and M. Rouabhia. 2001. Bronchial mucosa produced by tissue engineering: a new tool to study cellular interactions in asthma. *J. Allergy Clin. Immunol.* 107:36–40.
35. Chetty, A., P. Davis, and M. Infeld. 1995. Effect of elastase on the directional migration of lung fibroblasts within a three-dimensional collagen matrix. *Exp. Lung Res.* 21:889–899.
36. Cox, G., E. Kable, A. Jones, I. Fraser, F. Manconi, and M. D. Gorrell. 2003. Three-dimensional imaging of collagen using second harmonic generation. *J. Struct. Biol.* 141:53–62.
37. Freund, I., M. Deutsch, and A. Sprecher. 1986. Connective tissue polarity. Optical second-harmonic microscopy, crossed-beam summation, and small-angle scattering in rat-tail tendon. *Biophys. J.* 50:693–712.
38. Parry, D. A., and A. S. Craig. 1977. Quantitative electron microscope observations of the collagen fibrils in rat-tail tendon. *Biopolymers.* 16:1015–1031.
39. Plotnikov, S., V. Juneja, A. B. Isaacson, W. A. Mohler, and P. J. Campagnola. 2006. Optical clearing for improved contrast in second harmonic generation imaging of skeletal muscle. *Biophys. J.* 90:328–339.
40. Stoller, P., P. M. Celliers, K. M. Reiser, and A. M. Rubenchik. 2003. Quantitative second-harmonic generation microscopy in collagen. *Appl. Opt.* 42:5209–5219.
41. Stoller, P., B. M. Kim, A. M. Rubenchik, K. M. Reiser, and L. B. Da Silva. 2002. Polarization-dependent optical second-harmonic imaging of a rat-tail tendon. *J. Biomed. Opt.* 7:205–214.
42. Stoller, P., K. M. Reiser, P. M. Celliers, and A. M. Rubenchik. 2002. Polarization-modulated second harmonic generation in collagen. *Biophys. J.* 82:3330–3342.
43. Williams, R. M., W. R. Zipfel, and W. W. Webb. 2005. Interpreting second-harmonic generation images of collagen I fibrils. *Biophys. J.* 88:1377–1386.
44. Yeh, A. T., B. Choi, J. S. Nelson, and B. J. Tromberg. 2003. Reversible dissociation of collagen in tissues. *J. Invest. Dermatol.* 121:1332–1335.

45. Kim, B. M., J. Eichler, K. M. Reiser, A. M. Rubenchik, and L. B. Da Silva. 2000. Collagen structure and nonlinear susceptibility: effects of heat, glycation, and enzymatic cleavage on second harmonic signal intensity. *Lasers Surg. Med.* 27:329–335.

46. Lin, S. J., R. Wu, Jr., H. Y. Tan, W. Lo, W. C. Lin, T. H. Young, C. J. Hsu, J. S. Chen, S. H. Jee, and C. Y. Dong. 2005. Evaluating cutaneous photoaging by use of multiphoton fluorescence and second-harmonic generation microscopy. *Opt. Lett.* 30:2275–2277.

47. Han, M., L. Zickler, G. Giese, M. Walter, F. H. Loesel, and J. F. Bille. 2004. Second-harmonic imaging of cornea after intrastromal femtosecond laser ablation. *J. Biomed. Opt.* 9:760–766.

48. Lo, W., S. W. Teng, H. Y. Tan, K. H. Kim, H. C. Chen, H. S. Lee, Y. F. Chen, P. T. So, and C. Y. Dong. 2006. Intact corneal stroma visualization of GFP mouse revealed by multiphoton imaging. *Microsc. Res. Tech.*

49. Lyubovitsky, J. G., J. A. Spencer, T. B. Krasieva, B. Andersen, and B. J. Tromberg. 2006. Imaging corneal pathology in a transgenic mouse model using nonlinear microscopy. *J. Biomed. Opt.* 11:014013.

50. Morishige, N., W. M. Petroll, T. Nishida, M. C. Kenney, and J. V. Jester. 2006. Noninvasive corneal stromal collagen imaging using two-photon-generated second-harmonic signals. *J. Cataract Refract. Surg.* 32:1784–1791.

51. Tan, H. Y., S. W. Teng, W. Lo, W. C. Lin, S. J. Lin, S. H. Jee, and C. Y. Dong. 2005. Characterizing the thermally induced structural changes to intact porcine eye, part 1: second harmonic generation imaging of cornea stroma. *J. Biomed. Opt.* 10:054019.

52. Teng, S. W., H. Y. Tan, J. L. Peng, H. H. Lin, K. H. Kim, W. Lo, Y. Sun, W. C. Lin, S. J. Lin, S. H. Jee, P. T. So, and C. Y. Dong. 2006. Multiphoton autofluorescence and second-harmonic generation imaging of the ex vivo porcine eye. *Invest. Ophthalmol. Vis. Sci.* 47:1216–1224.

53. Wang, B. G., and K. J. Halbhuber. 2006. Corneal multiphoton microscopy and intratissue optical nanosurgery by nanojoule femtosecond near-infrared pulsed lasers. *Ann. Anat.* 188:395–409.

54. Torkian, B. A., A. T. Yeh, R. Engel, C. H. Sun, B. J. Tromberg, and B. J. Wong. 2004. Modeling aberrant wound healing using tissue-engineered skin constructs and multiphoton microscopy. *Arch. Facial Plast. Surg.* 6:180–187.

55. Brown, E., T. McKee, E. diTomaso, A. Pluen, B. Seed, Y. Boucher, and R. K. Jain. 2003. Dynamic imaging of collagen and its modulation in tumors in vivo using second-harmonic generation. *Nat. Med.* 9:796–800.

56. Wood, G. C., and M. K. Keech. 1960. The formation of fibrils from collagen solutions. 1. The effect of experimental conditions: kinetic and electron-microscope studies. *Biochem. J.* 75:588–598.

57. Silver, F. H., and D. E. Birk. 1984. Molecular structure of collagen in solution: comparison of types I, II, III, and IV. *Int. J. Biol. Macromol.* 6:125–132.

58. Silver, F. H., J. W. Freeman, and G. P. Seehra. 2003. Collagen self-assembly and the development of tendon mechanical properties. *J. Biomech.* 36:1529–1553.

59. Yuan, L., and A. Veis. 1973. The self-assembly of collagen molecules. *Biopolymers.* 12:1437–1444.

60. Nemethy, G. 1988. Energetics and thermodynamics of collagen self-assembly. *In* Collagen. M. E. Nimni, editor. CRC Press, Boca Raton, FL. 79–94.

61. McPherson, J. M., D. G. Wallace, S. J. Sawamura, A. Conti, R. A. Condell, S. Wade, and K. A. Piez. 1985. Collagen fibrillogenesis in vitro: a characterization of fibril quality as a function of assembly conditions. *Coll. Relat. Res.* 5:119–135.

62. Sheu, M. T., J. C. Huang, G. C. Yeh, and H. O. Ho. 2001. Characterization of collagen gel solutions and collagen matrices for cell culture. *Biomaterials.* 22:1713–1719.

63. Raeber, G. P., M. P. Lutolf, and J. A. Hubbell. 2005. Molecularly engineered PEG hydrogels: a novel model system for proteolytically mediated cell migration. *Biophys. J.* 89:1374–1388.

64. Zar, J. H. 1999. Biostatistical Analysis. Prentice-Hall Canada, Toronto, CA.

65. Hsu, S., A. M. Jamieson, and J. Blackwell. 1994. Viscoelastic studies of extracellular matrix interactions in a model native collagen gel system. *Biorheology.* 31:21–36.

66. Carroll, E. P., J. S. Janicki, R. Pick, and K. T. Weber. 1989. Myocardial stiffness and reparative fibrosis following coronary embolisation in the rat. *Cardiovasc. Res.* 23:655–661.

67. Discher, D. E., P. Janmey, and Y. L. Wang. 2005. Tissue cells feel and respond to the stiffness of their substrate. *Science.* 310:1139–1143.

68. Yeung, T., P. C. Georges, L. A. Flanagan, B. Marg, M. Ortiz, M. Funaki, N. Zahir, W. Ming, V. Weaver, and P. A. Janmey. 2005. Effects of substrate stiffness on cell morphology, cytoskeletal structure, and adhesion. *Cell Motil. Cytoskeleton.* 60:24–34.

69. Engler, A. J., S. Sen, H. L. Sweeney, and D. E. Discher. 2006. Matrix elasticity directs stem cell lineage specification. *Cell.* 126:677–689.

70. Zaman, M. H., L. M. Trapani, A. Siemeski, D. Mackellar, H. Gong, R. D. Kamm, A. Wells, D. A. Lauffenburger, and P. Matsudaira. 2006. Migration of tumor cells in 3D matrices is governed by matrix stiffness along with cell-matrix adhesion and proteolysis. *Proc. Natl. Acad. Sci. USA.* 103:10889–10894.

71. Rosenblatt, J., B. Devereux, and D. G. Wallace. 1994. Injectable collagen as a pH-sensitive hydrogel. *Biomaterials.* 15:985–995.

72. Christiansen, D. L., E. K. Huang, and F. H. Silver. 2000. Assembly of type I collagen: fusion of fibril subunits and the influence of fibril diameter on mechanical properties. *Matrix Biol.* 19:409–420.

73. Mertz, J., and L. Moreaux. 2001. Second-harmonic generation by focused excitation of inhomogeneously distributed scatterers. *Opt. Commun.* 196:325–330.

74. Sell, D. R., and V. M. Monnier. 1989. Isolation, purification, and partial characterization of novel fluorophores from aging human insoluble collagen-rich tissue. *Connect. Tissue Res.* 19:77–92.

75. Campagnola, P. J., H. A. Clark, W. A. Mohler, A. Lewis, and L. M. Loew. 2001. Second-harmonic imaging microscopy of living cells. *J. Biomed. Opt.* 6:277–286.

76. Helmchen, F., and W. Denk. 2005. Deep tissue two-photon microscopy. *Nat. Methods.* 2:932–940.

77. Roeder, B. A., K. Kokini, J. E. Sturgis, J. P. Robinson, and S. L. Voytik-Harbin. 2002. Tensile mechanical properties of three-dimensional type I collagen extracellular matrices with varied microstructure. *J. Biomech. Eng.* 124:214–222.

78. Migneault, I., C. Dartiguenave, M. J. Bertrand, and K. C. Waldron. 2004. Glutaraldehyde: behavior in aqueous solution, reaction with proteins, and application to enzyme crosslinking. *Biotechniques.* 37: 790–796, 798–802.

79. Nimni, M. E., D. T. Cheung, B. Strates, M. Kodama, and K. Sheikh. 1988. Bioprosthesis derived from cross-linked and chemically modified collagenous tissues. *In* Collagen. M. E. Nimni, editor. CRC Press, Boca Raton, FL. 1–38.

80. Jastrzebska, M., R. Wrzalik, A. Kocot, J. Zalewska-Rejdak, and B. Cwalina. 2003. Raman spectroscopic study of glutaraldehyde-stabilized collagen and pericardium tissue. *J. Biomater. Sci. Polym. Ed.* 14:185–197.